Journal of Marine Research, 57, 585–612, 1999

Experiments on waves trapped over the continental slope and shelf in a continuously stratified rotating ocean, and their incidence on a canyon

by Daniel L. Codiga[1], Dominique P. Renouard[2] and Adam M. Fincham[2]

ABSTRACT

Continental margins form a waveguide for topographic Rossby waves, which can be trapped to the bottom by continuous stratification and concentrated over the continental slope while propagating along the coast. We present results of laboratory wave simulations designed to keep as many dimensionless numbers (Rossby, Burger, normalized frequency, wave steepness, geometrical, Ekman, and Reynolds) as possible similar to those of coastal-trapped waves, such as are observed in coastal regions around the world. The 13-m diameter rotating tank is salt-stratified and a continental slope joins a shallow shelf region along the outer tank circumference to a deep central region. The velocity field is measured using a correlation-based digital particle image velocimetry technique at several depths. Current ellipses downstream from subinertial forcing indicate along-isobath propagation with energy concentrated at depth and three-dimensional structure in agreement with a numerical wave solution calculated using the experimental geometry, rotation rate, and buoyancy frequency. Contrasting the inviscid wave solution, experimental flow shows an asymmetry with positive time-mean $\overline{uv}$ correlations (u across isobaths toward deep water, v along isobaths with shallow water to the left), and phase variations perpendicular to isobaths with flow near the shelf break leading that farther inshore and offshore. Both of these attributes have been seen previously in ocean observations and are interpreted as the signature of frictional influences based on stratified slope-Kelvin wave behavior. When incident on a canyon that indents the slope and shelf, a wave propagates in to and out of it along isobaths while remaining concentrated over the sloping topography with only weakly modified amplitude and phase structure. Based on the limited range of parameter space studied, the implication is that alongshore wave propagation will remain largely unmodified by natural corrugations in the slope and shelf and loss of energy by scattering will be weak.

1. Introduction

Along many coastlines around the world, energetic current fluctuations with periods in the range of days to weeks are observed to propagate alongshore over the continental slope and shelf. There is an extensive literature that documents these signals, which may be excited by storms having occurred great distances away, and demonstrates their favorable comparison with linear coastal-trapped wave solutions (Brink, 1991, gives a review).

1. Department of Marine Sciences, University of Connecticut, 1084 Shennecossett Road, Groton, Connecticut, 06340-6097, U.S.A. ***email: codiga@oceans.dms.uconn.edu***

2. Equipe Coriolis, Laboratoire des Ecoulements Géophysiques et Industriels, Institut de Mecanique de Grenoble, Grenoble 38041, France.

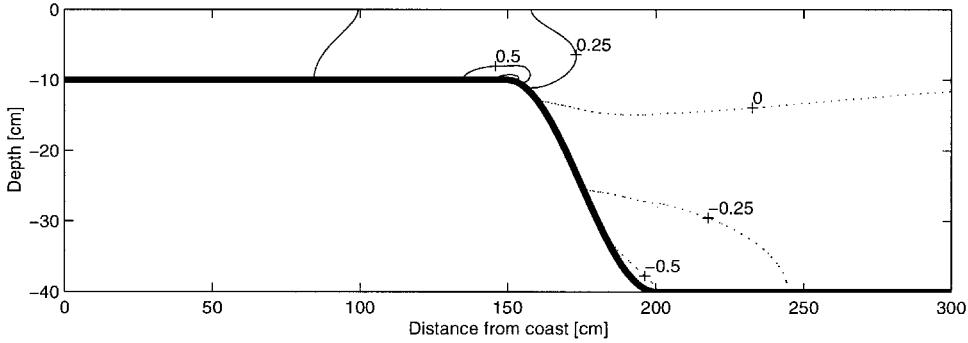

Figure 1. Trapped wave modal structure function for along-isobath current (see Eq. 3) calculated for laboratory parameters (Table 1) and normalized by the maximum value occurring on the bottom at the shelf break. Wave energy is concentrated near the bottom and over the shelf break and continental slope, and the baroclinic vertical structure includes a nearly horizontal nodal line (zero contour) just deeper than shelf break.

Dispersion properties and modal structures of the waves are typically calculated numerically using a formulation (Brink and Chapman, 1987) that incorporates the observed vertical profile of density stratification and a representative across-shore bathymetric profile, but does not account for variations in the direction along the coastline. Inclusion of alongshore nonuniformities that are ubiquitous in nature, such as submarine canyons, makes wave theory largely intractable and has motivated numerical simulations (e.g., Wilkin and Chapman, 1990) of scattering due to changes in coastline and topography. A laboratory experiment using an idealized shelf-slope geometry includes the physical effects that control wave dynamics and seems appropriate not only to verify wave theory over uniform bathymetry but also to address the effects of a canyon.

In this paper subinertial waves trapped over a continental slope and shelf are studied by means of rotating-table laboratory simulations that include continuous density stratification. We make a direct comparison between the detailed three-dimensional structure of current ellipses in the laboratory flow, in which wave energy concentrates near the bottom due to the stratification, and a linear free wave solution calculated numerically using experimental shelf-slope geometry, rotation rate and stratification. Asymmetries in the measured current ellipses that are not present in the free wave solution occur with the same sense as in ocean observations (Daifuku and Beardsley, 1983; Crawford and Thomson, 1984; Codiga and Eriksen, 1997) and are interpreted in terms of frictional influences on the basis of recent analysis of damped stratified slope-Kelvin wave modes (Codiga, 1997). In addition, we discuss results of an experiment to assess the strength and nature of modifications to a wave that is incident on a canyon cutting across the continental slope and shelf.

The focus here is on waves in relatively strong stratification, which can cause velocities to be strongest over the continental slope and shelf break so that the coastal boundary has little influence (Fig. 1). This may be understood in terms of bottom-trapped topographic

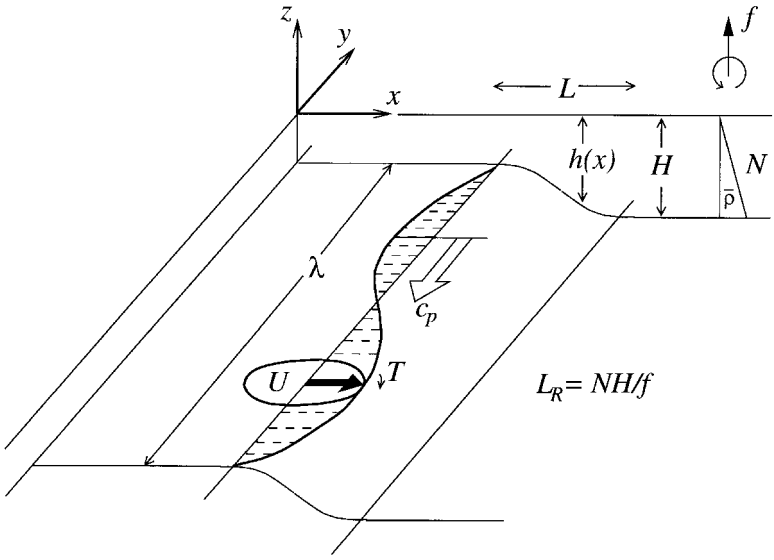

Figure 2. Diagram showing characteristic wave scales, system parameters, and coordinate axes.

Rossby waves (Rhines, 1970) within the waveguide that is centered on the continental slope because it is bounded by shallower and deeper regions having less steep slopes (Codiga, 1997). It is expected that the results here may also be pertinent to waves in weaker stratification, because for coastal-trapped waves the coastal wall often plays a more minor dynamical role than the depth variations of the continental slope. Consistent with this interpretation, in the numerical work of Wilkin and Chapman (1990) alongshore changes in the shelf-slope bathymetric profile caused more severe scattering than variation in the position of the coast.

In the next section, dynamical similitude between the experiment and the ocean is discussed. Section 3 describes the experimental approach. Results for uniform alongshore bathymetry and for incidence on a canyon are presented in Sections 4 and 5, respectively, and discussed in Section 6.

2. Wave dynamics and laboratory similitude with the ocean

Wave physics are controlled by (1) background rotation, (2) continuous density stratification, and (3) across-shore depth variations of the continental slope and shelf, in which a relatively steep topographic gradient is bounded on its shallow and deep sides by less steep inclines. The idealized experimental system includes these dominant effects and consists of a uniformly rotating, uniformly stratified ocean with a cosine-squared depth profile joining flat shallow and deep regions (Fig. 2). We consider a stratification that is uniform in depth, with the reasonable expectation that vertical variations in stratification

Table 1. Characteristic wave scales and parameter values for coastal ocean and the central experiment.

	Coastal Ocean	Experiment
Coriolis parameter, f	10^{-4} s^{-1}	0.126 s^{-1}
Buoyancy frequency, N	10^{-3} s^{-1}	0.55 s^{-1}
Continental slope width, L	30 km	50 cm
Offshore depth, H	3000 m	40 cm
Rossby radius, $L_R = NH/f$	30 km	175 cm
Wave frequency, σ	2.4×10^{-5} s^{-1}	0.101 s^{-1}
Wavelength, $\lambda = 2\pi/l$	≈800 km	650 cm
Phase speed, $c_p = \sigma/l$	≈3 m/s	9.7 cm/s
Current, U	≈10 cm/s	0.4 cm/s
Diffusivity, K_V	≈20 cm^2/s	0.01 cm^2/s

strength on the order of those typically observed over the continental slope and shelf would not be likely to qualitatively change the results. Absence of the beta effect in the lab is consistent with wave theory where it is generally neglected relative to the potential vorticity gradient associated with depth variations.

Characteristic parameters describing the system (Fig. 2) begin with the background rotation, of Coriolis parameter f (positive, Northern hemisphere), and the rest-state stratification, having buoyancy frequency N. The horizontal scale L is the across-isobath width of the slope and L_R is the first baroclinic Rossby radius of deformation, given by NH/f where H is the depth of the deep ocean. Waves have along-isobath wavelength λ and period $T = 2\pi/\sigma$, where σ is frequency. Currents propagate at phase speed c_p alongshore with the coast to their right, and are dominantly horizontal with typical magnitude U. Although these scales vary widely among the diverse coastal ocean settings around the world, reasonable characteristic values for them and for the vertical eddy momentum diffusivity, K_V, are known (Table 1, first column). The Coriolis parameter chosen pertains to midlatitudes, the buoyancy frequency to shallow thermocline depths, the wave frequency to a period of a few days as appropriate to storm-driven fluctuations, and K_V to estimates based on microstructure measurements over the shelf. The corresponding set of parameter values for the central experiment (Table 1, second column) include the molecular viscosity of water for K_V, implications of which are described later in this section.

Dimensionless numbers (Table 2) formed using these values guided the design of the experiment and ensure the similitude of the nearly inviscid dynamics between the laboratory and oceanic flows. As appropriate for subinertial waves supported by and trapped to sloping bottom topography at frequencies for which free internal waves cannot exist, the normalized wave frequency σ/f is less than one. There are two measures of wave nonlinearity, the Rossby number $Ro = U/(fL)$ and the wave steepness U/c_p, or equivalently the ratio UT/λ between particle orbit length and wavelength; both have been kept small in the experiment as appropriate to best model oceanographic observations of coastal-trapped

Table 2. Nondimensional numbers, formed using values in Table 1, to assess similitude between experiment and coastal ocean.

	Coastal Ocean	Experiment
Normalized wave frequency, σ/f	0.24	0.8
Rossby number, $Ro = U/(fL)$	0.03	0.06
Wave steepness, U/c_p	0.03	0.04
Burger number, $S = (NH/(fL))^2$	1	12
Slope-width/wavelength, L/λ	0.04	0.08
Ekman number, $Ek = 2K_V/(fH^2)$	4×10^{-5}	10^{-4}
Reynolds number, $Re = UL/K_V$	1.5×10^6	2×10^3

waves. The Burger number $S = (NH/(fL))^2$ is the squared ratio of the Rossby radius to the slope width. In the experiment it is higher than the representative oceanic value, though within the range of values spanning natural geographic variations, indicating that the laboratory flow represents a relatively strong oceanic stratification. Wave dispersion properties depend on the aspect ratio H/L and ratio of buoyancy and Coriolis frequencies N/f only through their combined control of the Burger number; in the simulation, exaggeration of the aspect ratio is compensated by a relatively low N/f ratio. As it is in nature, in the experiment the ratio L/λ between shelf width and along-isobath wavelength is much smaller than one.

One advantage of the large 13 m diameter of the Coriolis/LEGI-IMG platform over a more standard 1 m diameter rotating table is that the dimensionless numbers gauging viscous effects are brought closer to their oceanic values. The Ekman number $Ek = 2K_V/(fH^2)$ is the squared ratio of boundary layer thickness to total depth. In laboratory simulations, even though Ekman layers remain a small fraction of the total depth, Ek tends to exceed oceanic values as constrained by the molecular viscosity of water and the scale of the experiment. The 13 m table allows the total depth to be increased relative to a smaller table, for given values of the other dimensionless numbers, hence a reduction of the Ekman number by as much as an order of magnitude. This improvement is significant but can still leave the Ekman number as much as an order of magnitude higher than representative oceanic values, though this is not the case for flow in shallow shelf regions where boundary layers can occupy a substantial portion of the total depth. Following standard scaling arguments, the Ekman layer is expected to dominate dissipative effects on the waves. However, a Reynolds number $Re = UL/K_V$, defined using the eddy viscosity in the vertical direction because it is thought more important to wave dissipation on oceanic scales than that in the horizontal, can also be used to compare laboratory and ocean flows. For given Rossby and Burger numbers, the 13 m table allows larger length scales and velocities so that the Reynolds number may be increased by more than an order of magnitude. Although the result is nearer the oceanic estimate than for a smaller experiment, it remains low by a few orders of magnitude. The experiment is not expected to model oceanic dissipative processes with a high degree of realism because of this limitation, but its large size

minimizes unrealistic frictional influences so that the nearly inviscid wave dynamics are captured more accurately.

The linearized, inviscid, Boussinesq, and hydrostatic momentum, density conservation, and continuity equations governing the waves are

$$u_t - fv = -p_x \tag{1a}$$

$$v_t - fu = -p_y \tag{1b}$$

$$0 = -p_z + b \tag{1c}$$

$$b_t + N^2 w = 0 \tag{1d}$$

$$u_x + v_y + w_z = 0 \tag{1e}$$

where subscripts indicate partial differentiation. The system has Cartesian coordinates (x, y, z) and corresponding velocity components (u, v, w) in the directions positive across isobaths toward deeper water, positive along isobaths with shallow water on the left, and positive upward respectively (Fig. 2). The buoyancy frequency of the rest-state background stratification is defined by $N^2 = (-g/\rho_o)(d\overline{\rho}/dz)$, where g is gravitional acceleration and $\overline{\rho}$ is the density deviation from the constant reference density ρ_o. As are (u, v, w), the reduced pressure p (pressure divided by ρ_o) and the buoyancy b (density perturbation multiplied by $-g/\rho_o$) are perturbations about the stationary rest state. The surface is at $z = 0$, the coast is at $x = 0$, and the depth h varies in the x direction only, as

$$h(x) = \begin{cases} h_o & \text{for } x \le X_{sb} \\ H - (H - h_o)\cos^2[(\pi/2)(x - X_{sb})/L] & \text{for } X_{sb} < x < X_{sb} + L \\ H & \text{for } x \ge X_{sb} + L\,. \end{cases}$$

The cosine-squared profile of width L joins the shelf, of depth h_o and with shelf break distance from the coast X_{sb} (10 cm and 150 cm respectively in the experiment, Fig. 1), to the deep ocean of depth H. Appropriate boundary conditions include decay of wave variables at large distance from the slope, a rigid lid at the surface, and the kinematic condition of no flow perpendicular to the boundary both at the vertical coastal wall and at the sea floor. The lattermost condition,

$$w + uh_x = 0 \qquad \text{at } z = -h(x) \tag{2}$$

is the most important dynamical control and captures the elemental physics (Rhines, 1970), since the coastal wall has little influence on waves (Fig. 1) whose energy concentrates at depth and over the slope.

For a given stratification strength and topographic profile, dispersion properties and modal structures are determined by taking variables p, u, v, w, b of the form, for example using the along-isobath flow,

$$v(x, y, z, t) = \mathscr{R}\{\tilde{v}(x, z)\exp[i(ly - \sigma t)]\}. \tag{3}$$

Here, $\tilde{v}(x, z)$ is the modal structure function, $l = -2\pi/\lambda$ is the along-isobath wavenumber (negative because propagation occurs with shallow water to the right), and $\mathscr{R}$ indicates taking the real part. The equation for the modal structure function that results from substitution of form (Eq. 3) for all variables into the system (1,2) is solved numerically (Brink and Chapman, 1987), as is required for topographic profiles having all except for the most idealized analytic shapes (Huthnance, 1978). In inviscid free waves u and v are in quadrature such that at a fixed location the flow rotates in time and sweeps out open current ellipses; at locations in the cross-isobath/vertical plane that have clockwise-in-time rotary currents, as tends to be the case where modal amplitudes are largest, the sense of along-isobath phase propagation (Eq. 3) means that instantaneous flow vectors turn counterclockwise in the direction of propagation (e.g., see: Huthnance, 1978; Codiga, 1997).

The wave solution using laboratory parameters is dominated by horizontal velocities that are concentrated at depth and over the continental slope and shelf break, and has low vertical-mode baroclinic structure, as revealed by the modal structure function for along-isobath velocity (Fig. 1). Except for its bottom intensification, because it is supported by and strongest over the continental slope and is nearly independent of the coastal wall the wave is analogous to a double Kelvin wave (e.g. Longuet-Higgins, 1968; Chapman, 1982). The frequency and along-isobath wavenumber of the mode in Figure 1 are from the free wave dispersion curve to be discussed in Section 4, and correspond closely with the experimental forcing frequency and the wavelength determined by direct measurement in the central experiment.

3. Experimental approach and analysis

In the experiment the outer perimeter of the cylindrical tank, a shallow flat region representing the continental shelf, is joined to the flat deep central region by a continental slope with isobaths having constant radial distance from the axis of rotation (Fig. 3, plan view). The tank is filled with a continuous salt stratification from the bottom up by a mixing method using fresh and salty reservoirs. This is done over a four-hour period after the tank has begun rotating counterclockwise with angular velocity $f/2$ (Table 1); these conditions are thought to make spin-up more efficient both by requiring water to enter the tank through the bottom Ekman layer and by maximizing the time spent within it. Small gaps along vertical seams in the fiberglass topographic surface allow water to pass through at a few azimuths, filling the volume below the topography as well as that above it so that the final stratification is depth independent despite the changes in above-topography area with depth. The surface paraboloid causes a 1.7 cm surface height at the outer tank wall relative to that at the axis of rotation, and the 0.2 cm height difference across the 50 cm width of the continental slope where the flow of interest occurs is neglected relative to the total depth of between 10 and 40 cm. After an undisturbed overnight period, the spin-up to solid body rotation is complete. Wind effects are minimized by radially oriented cloths hung vertically above the water surface along the outer tank perimeter, and large flat foam floats tethered to

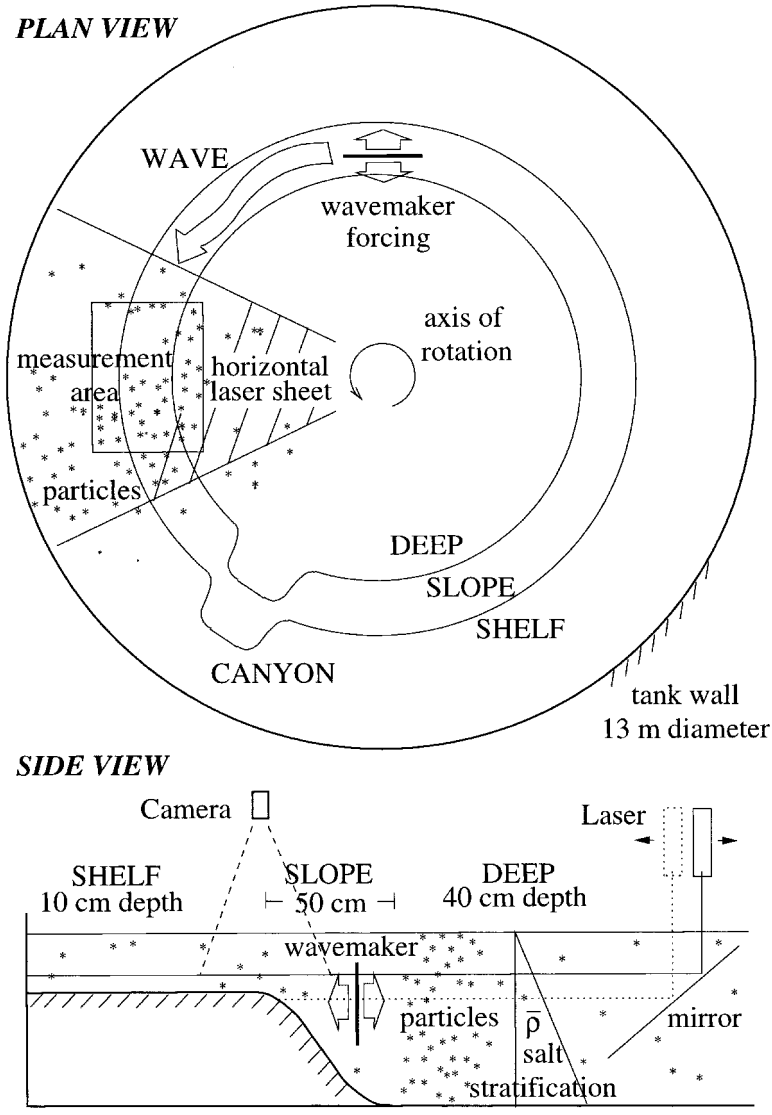

Figure 3. Schematic of laboratory configuration. The canyon is present only for experiments discussed in Section 5.

the tank that cover most of the surface area. After spin-up, residual motions are reduced to less than 0.05 cm/s, except where a clockwise mean current reaches 0.17 cm/s in the shallowest few cm of the tank. Neither the surface floats nor the near-surface residual flow contaminate or cause excessive frictional damping to the wave signal of interest because it is concentrated near the bottom.

As an idealized representation of a storm-driven disturbance, a wavemaker oriented along isobaths is positioned over the sloping region and oscillates in the direction perpendicular to isobaths, exciting waves that move away with shallow water to their right (Fig. 3, side view). The focus of the experiment is motions about one wavelength or farther away from the wavemaker, which are interpreted as a locally unforced, single along-isobath wavenumber, damped wave that has been excited remotely. It will be demonstrated later in this section that the amplitude of the component of the response not at the dominant along-isobath wavenumber is weak. The wavemaker is driven continously during experimentation, and flow is measured after an equilibrium state is reached having waves propagating throughout the tank along isobaths over the region of sloping topography. Because the flow is periodic, its structure is determined by combining nonsimultaneous measurements from several depths, each referenced in time relative to the phase of the wavemaker. The efficiency of the wavemaker is low so currents in the measurement area centered 605 cm away along the slope in the direction of wave propagation are typically about one third as strong as those forced at the wavemaker; basin-wide resonances do not occur because a wave incident on the wavemaker after completing a circuit around the entire tank is too weak relative to the wavemaker forcing. The wavemaker is 1 m long and 20 cm high, its upper edge is submerged by 2.5 cm (Fig. 3, side view), and it moves with a fixed period T and amplitude to force horizontal flow of u_F. In the central experiment $T = 62.3$ s, corresponding to $\sigma/f = 0.8$, and $u_F = 1.5$ cm/s. Density profiles show no significant changes after several days of experimentation, indicating that any mixing caused by the wavemaker affects a negligible volume fraction of the tank and leaves the basic stratification unmodified.

The three-dimensional structure of horizontal currents is measured noninvasively using the digital particle image velocimetry system described by Fincham and Spedding (1997). Polystyrene Huntsman particles of nominal diameter 0.7 mm, after first being given the correct densities by expansion in a hot water bath, are seeded during spin-up throughout the tank at all depths and remain neutrally buoyant at a number density such that the rms separation distance is about 0.4 cm. An Argon laser beam at 6 W power is spread by an oscillating mirror and reflected off a submerged 45° mirror fixed in the tank (Fig. 3, side view) to illuminate the advection of particles within a 1-cm thick horizontal layer. The depth of flow illuminated is controlled by repositioning the laser horizontally. The velocity field is measured in a 150 cm by 200 cm area over the sloping region by capturing a sequential image pair from a Pulnix digital camera mounted directly above the flow. Vectors on a grid with 3.9 cm resolution (Fig. 4, to be described below) are determined by cross-correlations between subregions of the image pairs centered on each gridpoint. In making the measurement no assumption is made regarding the horizontal divergence of the flow. Fincham and Spedding (1997) explain in detail the methods and software analysis applied to interpolate and spectrally filter the correlation results and give the velocities seen in Figure 4. Together with the system for controlling the hardware and sampling parameters, these techniques are collectively called Correlation Image Velocimetry (CIV).

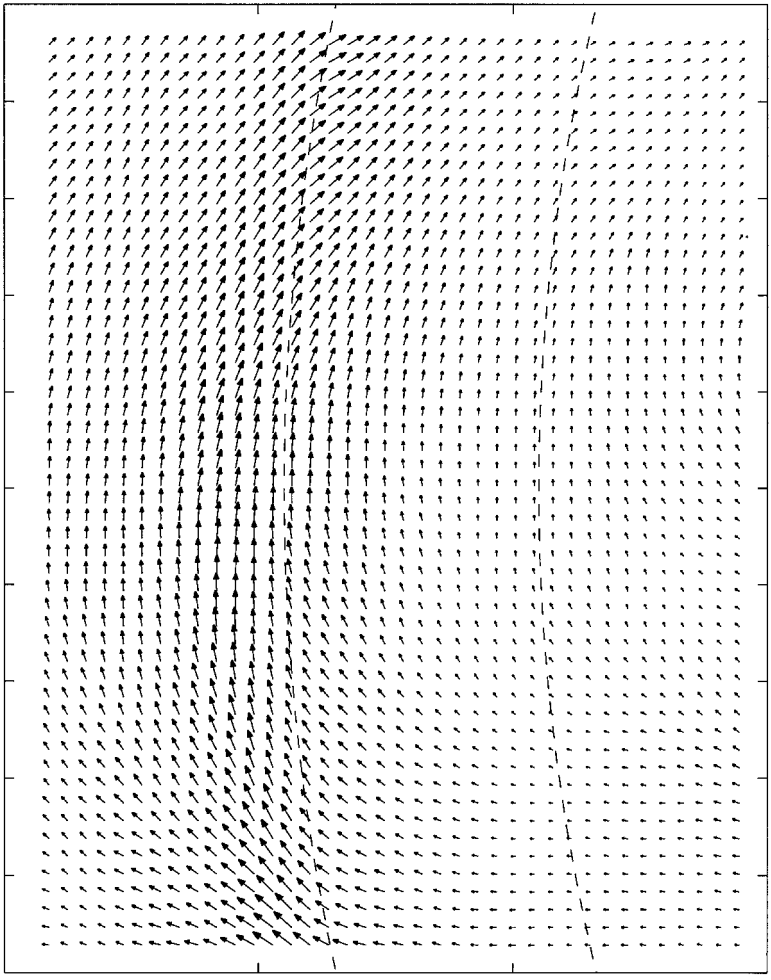

Figure 4. Plan view of instantaneous horizontal currents measured by the CIV correlation particle-image-velocimetry technique of Fincham and Spedding (1997), at 1 cm shallower than the shelf depth. The field of view is 150 cm by 200 cm and is centered at a location 605 cm away from the wavemaker center along isobaths (dashed lines: shelf break at left, base of slope at right) in the direction of wave propagation (Fig. 3). The grid resolution is 3.9 cm and the maximum velocity is $0.35u_F = 0.53$ cm/s. Evidence of waves propagating along isobaths includes the concentration of stronger currents over the shelf break and the counterclockwise turning of the velocity along isobaths along the propagation direction, from top to bottom in the figure.

A single CIV snapshot of the flow at a depth near the bottom over the shelf (Fig. 4) reveals two basic characteristics that are consistent with a trapped-wave mode propagating along isobaths. First, the velocity vector turns counterclockwise with increasing distance from the wavemaker along the shelf break, an indication of phase propagation along

isobaths away from the wavemaker as explained in Section 2. Second, the strongest currents are concentrated near the shelf break and there is weaker flow farther onto the shelf and in deeper water, as is seen in Figure 1.

In order to make a more complete comparison between the data collected and the u and v fields of the numerical wave solution described in the previous section, it will be necessary to (1) decompose the measured velocities into components along and across isobaths, and (2) assess how they change with distance along an isobath. For these reasons, all further analysis is done using (1) across- and along-isobath velocity components (u, v) determined relative to the local isobaths after (2) interpolating the raw CIV data (Fig. 4) from its Cartesian measurement grid onto an orthogonal curvilinear grid that follows isobaths. The original (Fig. 4) and interpolated (Fig. 5) grids have the same nominal spacing, which resolves well the scales of flow variations.

Horizontal current ellipses (Fig. 5) are determined by sampling the flow as shown in Figure 4, for example in the central experiment, ten times per period for two wave periods. Using the timeseries from each individual gridpoint and the known forcing frequency σ, least-squares fits minimizing the difference between the measured across- and along-isobath currents and the model functions

$$u_m = a^u \cos(\sigma t + \phi^u) + \hat{u}$$

$$v_m = a^v \cos(\sigma t + \phi^v) + \hat{v}$$

are made, respectively, to determine the amplitudes (a^u, a^v), phases (ϕ^u, ϕ^v), and residual currents ($\hat{u}$, $\hat{v}$), each a constant. Where the wave energy is concentrated, near the bottom, the residual currents are usually less than 5% and always less than 15% of the oscillatory amplitudes; as the residual is not of interest here, all further analysis focusses on the data after the residual has been removed, which is denoted (u_d,v_d). The difference between (u_d, v_d) and the model functions (u_m, v_m) is used to define the percent misfit variance for each fit as

$$[\varepsilon^2]^t = 100 \sum_t [(u_d - u_m)^2 + (v_d - v_m)^2] / \sum_t [u_d^2 + v_d^2].$$

Here, the superscript t indicates that the harmonic fit includes periodic time variations only and uses data from a fixed (x, y, z) location. The denominator is the total variance in the data, and the summations are over all points in the timeseries. The percent misfit variance $[\varepsilon^2]^t$ is in the range of 5 to 15% and typically less than 10%, an indication that the energy in the response at any given location is predominantly in a single sinusoid in time at the forced frequency as expected. The misfit variance captures all ambient random experimental fluctuations at frequencies other than that of the wavemaker. Therefore, when the question of whether a multiple wavenumber analysis is necessary is discussed later in this section, the limit on the ability of the data to resolve and isolate flow at the wavemaker frequency is taken to be $\overline{[\varepsilon^2]^t}$, where the overbar indicates an average along an isobath.

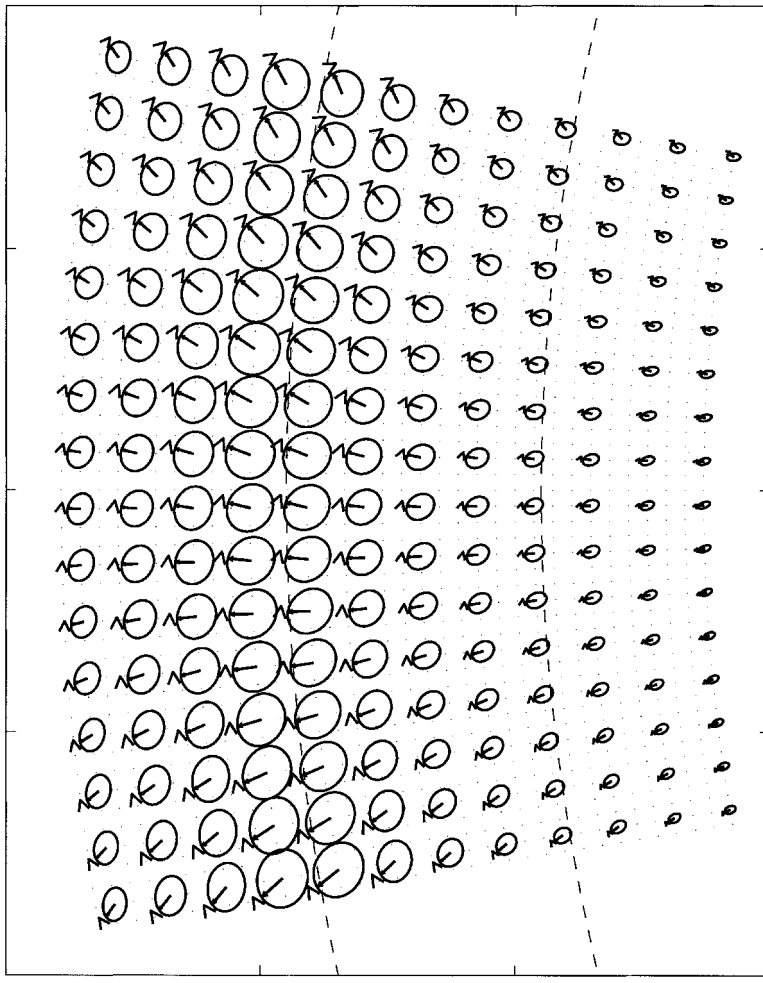

Figure 5. Plan view current ellipses measured 1 cm shallower than the shelf depth, calculated for each individual point from timeseries of data such as shown in Figure 4 after interpolation to the grid oriented along isobaths shown here. Only every third ellipse is shown. The field of view is the same as in Figure 4. The maximum velocity reaches $0.31u_F = 0.46$ cm/s. Each velocity vector sweeps out its ellipse in the direction marked near its head during one wave period.

In order to compare the laboratory flow over regions of slope-shelf profile that are uniform along isobaths to the wave solution (Eq. 3), a nonlinear least-squares fit to a single along-isobath propagating harmonic is made using the data (u_d, v_d) at a given depth from all locations in the measurement area along a given isobath. These are fit to along-isobath harmonic model functions

$$U_m = A^u \cos(ly - \sigma t + \Phi^u) \tag{4a}$$

$$V_m = A^v \cos(ly - \sigma t + \Phi^v) \tag{4b}$$

where y is the distance along the curving isobath. The fit determines amplitudes (A^u, A^v) and phases (Φ^u, Φ^v) at each (x, z) grid location in the across-isobath/vertical plane; the along-isobath wavenumber l is also determined by the fit. Use of the Gauss-Newton nonlinear optimization function in Matlab is made to calculate the fit. The percent misfit variance for each along-isobath harmonic fit is determined as

$$[\varepsilon^2]^{yt} = 100 \sum_{yt} [(u_d - U_m)^2 + (v_d - V_m)^2] / \sum_{yt} [u_d^2 + v_d^2].$$

In this case, the superscript yt indicates that the harmonic fit is to an along-isobath propagating harmonic and uses timeseries data from all positions along an isobath. The denominator is the total variance in the data and the summations are over all points in the timeseries and all points along the isobath. The percent misfit variance $[\varepsilon^2]^{yt}$ in this along-isobath fit ranges from 2 to 35%, is typically less than 15%, and reaches large values only at depths deeper than the shelf break and over deep water far from the shelf. As discussed in the next section, the wavenumbers determined in these fits are in agreement with that of a free wave mode at the wavemaker frequency on the dispersion curve determined for trapped waves (Eqs. 1, 2, 3) using experimental rotation rate, buoyancy frequency, and slope-shelf profile; the next-higher mode on a dispersion curve at the wavemaker frequency has a significantly larger wavenumber such that there is no ambiguity in which mode has been excited.

Motions at wavenumbers other than that in the along-isobath fit, while of course possible even though flow is dominantly at a single frequency, have amplitudes small enough that a more sophisticated analysis accounting for multiple wavenumbers is not warranted. Energy at other wavenumbers will appear as an increase in the percent misfit variance in the along-isobath harmonic fit, $[\varepsilon^2]^{yt}$, relative to the along-isobath average of the percent misfit variance in the time-periodic fits, $\overline{[\varepsilon^2]^t}$. This percent misfit in all wavenumbers other than the primary along-isobath harmonic,

$$\varepsilon^2 = [\varepsilon^2]^{yt} - \overline{[\varepsilon^2]^t},$$

has been calculated for flow over the uniform slope-shelf profile with no canyon present and also over the sections of unchanging slope-shelf profile both before and after wave incidence on the canyon when it is present. The main result is that, except at certain depths deeper than the shelf break and over deep water far from the shelf, the percent misfit in other wavenumbers ε^2 reaches just 0.4 times the level of precision for resolving the main signal, represented by $\overline{[\varepsilon^2]^t}$ as described above. Considering that energy at other wavenumbers does not exceed this basic measurement limitation, there is little motivation to carry out a higher-order analysis that includes multiple wavenumbers. Regarding those regions at depth and far offshore from the shelf break, where energy in other wavenumbers is somewhat increased, there are two points to be made. First, the amount of energy only rises to become comparable to $\overline{[\varepsilon^2]^t}$, itself a small fraction of the main wave, indicating that in a multiple wavenumber analysis a signal at a wavenumber different from the primary mode would not be clearly isolated from ambient fluctuations not at the wave frequency. Second,

as pertains to the possibility of scattered or evanescent waves of different wavenumber potentially generated by interaction with the canyon (Section 5), the measured structure and amplitude of the misfit ε^2 attributable to other wavelengths does not differ significantly among the measurements without the canyon, prior to incidence, and after incidence. This suggests that the small amount of energy at other wavelengths (1) is not caused by interaction with the canyon, because it is present in the experiment without the canyon, and (2) is not strongly modified by interaction with the canyon, because it is not significantly increased nor decreased before or after wave incidence on the canyon. The detailed mechanism of wave excitation local to the wavemaker is a potential explanation of this minor component of the flow, and because such a signal is not of interest and does not affect any of the conclusions of our study it is not pursued further.

4. Results: Propagation along uniform slope-shelf profile

This section presents results from a slope-shelf geometry that is uniform in the along-isobath direction of wave propagation. Results after a canyon is inserted in the tank will be described in the next section.

The three-dimensional structure of the measured laboratory flow may be concisely presented (Fig. 6) by plotting, at each point on a grid in the across-isobath/vertical plane, the horizontal current ellipse and instantaneous velocity vector that result from the fit to an along-isobath propagating harmonic (Eq. 4) using data at all points along the isobath. For example, in Figure 6 the row of ellipses 9 cm deep has been determined using the same data as was used in plotting all of Figure 5. The low increase in the misfit variance in the along-isobath harmonic fit relative to the time-dependent harmonic fits at individual locations (Section 3) confirms that the measured flow has structure dominated by a single wavenumber, as is visually apparent in the turning of the velocity vector along isobaths seen in Figure 5 prior to the fit.

The along-isobath wavelength measured is in agreement with that set by the wavemaker frequency and the dispersion curve for waves calculated numerically using the laboratory rotation rate, slope-shelf geometry, and buoyancy frequency (Fig. 7). In the region of Figure 6 where velocities are strongest, within 5 cm vertically of the shelf and within about 40 cm horizontally of the slope at depth, the along-slope wavelength determined by the fit varies between 490 cm and 710 cm and has kinetic-energy weighted average value 654 cm. This is consistent with the turning of the velocity vector by about 90 degrees over a distance of about 165 cm along the shelf-break isobath as seen in Figure 5. When the system (1–3) is solved numerically (Brink and Chapman, 1987) for laboratory parameters (Table 1), the family of dispersion curves (Fig. 7) includes on its gravest (highest-frequency) branch a wavenumber magnitude of 0.00933 cm^{-1} at the forced frequency. The corresponding wavelength of 673 cm is well within the range of estimates made from the data and near to their 654-cm average. The second-gravest dispersion curve is separated from the gravest by significant frequency and wavenumber differences. Within the range of wavenumbers corresponding to the measured wavelengths, frequencies on the gravest

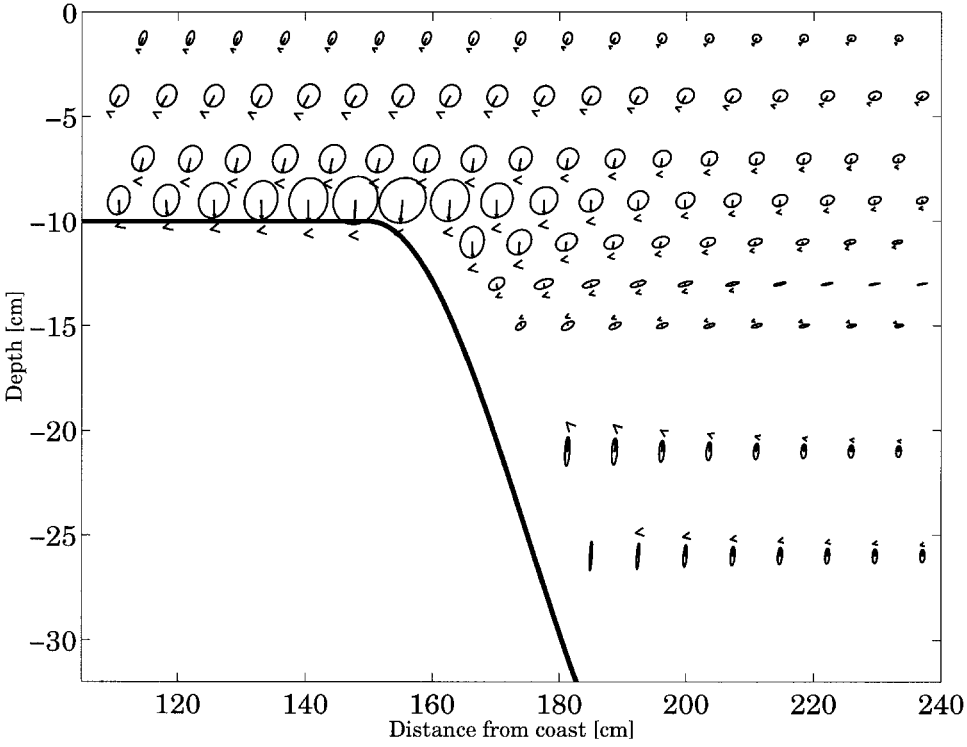

Figure 6. Structure in the across-isobath/vertical plane of horizontal current ellipses, each representing a fit to an along-isobath propagating harmonic (Eq. 4) using laboratory data from all points along the isobath at the cross-isobath position and depth of the ellipse center. Across- (along-) isobath flow $u(v)$ is positive rightward (upward), the maximum velocity reaches $0.30u_F$ = 0.45 cm/s, and for clarity only every second ellipse at each depth is shown. See text for full description.

curve are no lower than $0.75f$, in contrast to those on the second-gravest, which are less than $0.4f$; the second-gravest curve has wavelength of 180 cm at the forced frequency. Evidence that the gravest mode has been most strongly excited is consistent with the expectation that higher modes, of lower frequency and more complex spatial structure, are acted on more strongly by friction (to be quantified below) and have been less efficiently excited by the wavemaker. Energy at other wavelengths has been determined, and shown to be unimportant, by comparison between the misfit of along-isobath harmonics and the misfit of time-dependent harmonic fits at individual locations (Section 3).

Several distinct features are seen in the measured current ellipse structure of Figure 6. (i) The strongest velocities are concentrated near the bottom and over the shelf break and slope: shallower than the shelf, the peak currents are over the shelf break, with flow weakening both nearer the coast and toward deeper water; at depth over the slope, the strongest amplitudes occur near the boundary and currents weaken with distance away

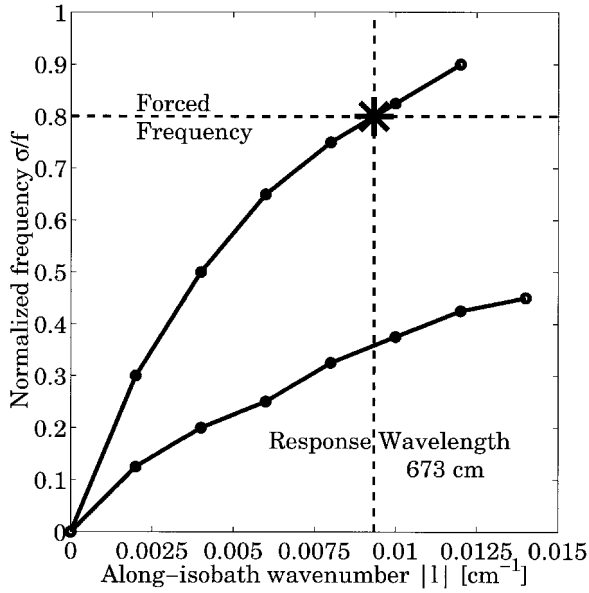

Figure 7. Dispersion curves calculated numerically for the laboratory stratification, rotation rate and slope-shelf geometry. The x-axis is the absolute value of the along-isobath wavenumber l. The wavenumber at the forced frequency on the gravest (highest frequency) mode curve corresponds to wavelength 673 cm, consistent with the value determined directly from experimental data.

from the slope. (ii) The instantaneous velocity vectors reveal the baroclinic structure of the flow, with the along-isobath flow at the time shown in Figure 6 in nearly opposite directions in horizontal layers above and below a depth a few cm below the shelf. (iii) Above the shelf depth, ellipses are nearly circular and rotate clockwise in time. (iv) Just deeper than the shelf, ellipses become elongated across isobaths and the direction of rotation changes from clockwise to counterclockwise with depth increasing past about 14 cm. (v) Deeper ellipses over the slope are elongated along isobaths and rotate counterclockwise in time. (vi) There is a systematic "tilt" of the current ellipses such that the time-mean correlation $\overline{uv}$ is positive.

Current ellipses of the inviscid free wave numerical solution corresponding to the gravest mode at the forced frequency (Fig. 8) have nearly all of the same detailed features as the observed lab flow, confirming that the response to the wavemaker is a trapped wave governed by the set of equations solved. Currents in Figure 8 are controlled by the modal structure function of both the along-isobath (Fig. 1) and across-isobath velocity components. The attributes (i)–(v) just described in the laboratory data are apparent in the free wave structure, and each is a fundamental characteristic of the trapped wave solution as has been shown in detail for the analogous system of trapped waves in stratification at a seamount (Codiga, 1997). Free waves of form (Eq. 3) have either imaginary or real (not complex) modal structure function, hence propagate only along isobaths and have purely

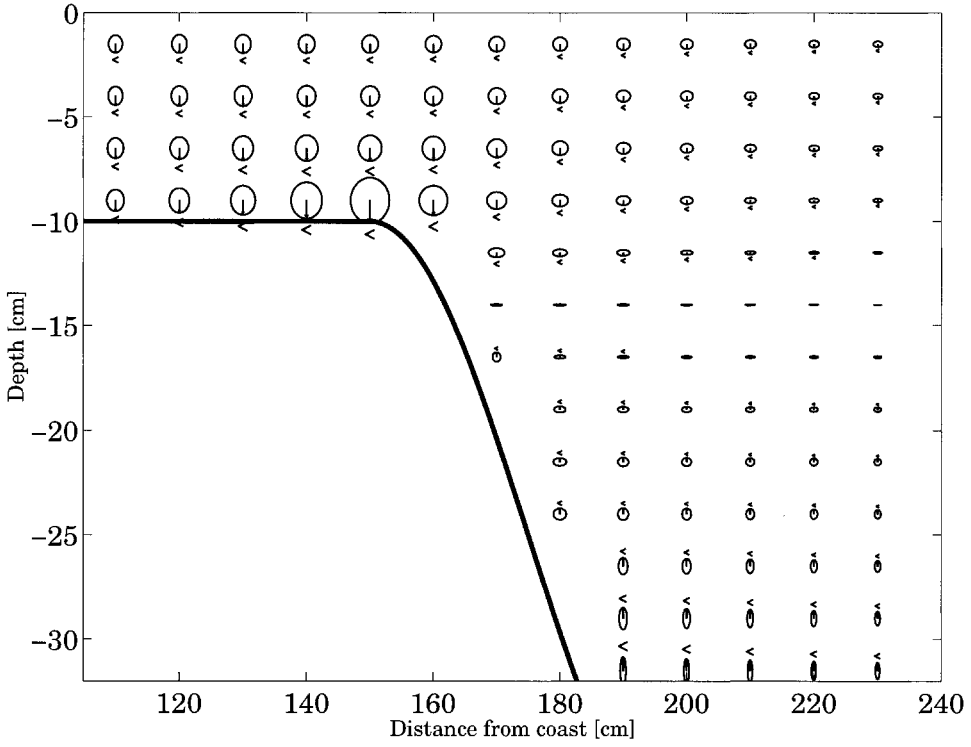

Figure 8. Current ellipse structure of inviscid free wave calculated numerically for laboratory frequency and wavenumber (asterisk, Fig. 7). The amplitude and phase are arbitrary, as with any linear solution, and have been chosen to facilitate a direct comparison to Figure 6. See text for discussion.

standing wave structure in both the across-isobath and vertical directions. This includes exact quadrature ($\overline{uv} = 0$) of the across- and along-isobath currents such that major and minor ellipse axes are parallel or perpendicular to isobaths. In strong stratification as considered here, the standing wave nature is expressed as vertically stacked, nearly horizontal regions in which currents rotate either clockwise or counterclockwise in time. These attributes can be understood in terms of ray theory for stratified slope-Kelvin wave rays (plane, propagating, f-plane topographic Rossby waves in stratification over a planar sloping bottom of Rhines, 1970) that are trapped between turning points in the waveguide formed by the continental slope because it is bounded by less steep slopes in shallower and deeper water (demonstrated schematically in Fig. 9 of Codiga, 1997).

One of the most prominent differences between the laboratory data (Fig. 6) and the free wave solution (Fig. 8) is the systematic tendency in the experiment for ellipses to lie at an angle to isobaths such that the correlation $\overline{uv} > 0$, which may be understood in terms of frictional influences which break the standing-wave symmetry of the inviscid free wave. Because they have been forced remotely by the wavemaker it is appropriate to interpret the

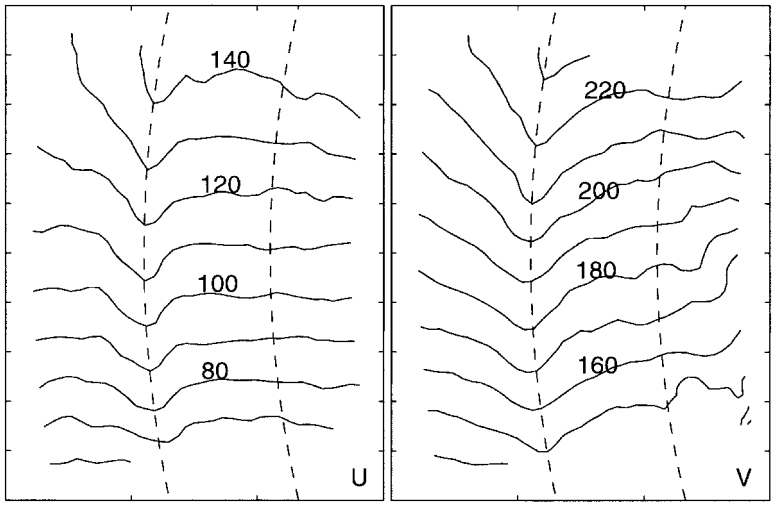

Figure 9. Contours of phase of the across- and along-isobath velocity components (left and right frames, respectively) for the data shown in Figure 5, in degrees. The field of view in each frame is the same as shown in Figure 5. The dominant signal is coherent phase propagation along isobaths (dashed lines) with u and v nearly 90° apart, and along a section perpendicular to isobaths the phase near the shelf break (left dashed line) leads the phase at points both further inshore and offshore.

currents measured in the experiment as unforced damped waves. A characteristic feature of trapped-wave solutions under the influence of frictional damping (Codiga, 1997) is current ellipses that are oriented at an angle to isobaths in the sense seen in the experiment. In terms of the upgoing and downgoing stratified slope-Kelvin waves whose superposition forms the across-isobath standing wave structure, friction which is strongest where the velocities are greatest breaks the symmetry such that the wave carrying energy toward the dissipative region dominates. In an analysis of trapped wave observations, Codiga and Eriksen (1997) noted the occurrence of this asymmetric current ellipse signature in field measurements.

Wave decay in the direction of propagation is relatively weak based on the fractional reduction of amplitude within the measurement field of view, and this is in reasonable agreement with results of a perturbation method (Brink, 1990) using linear bottom stress parameterization and the numerically determined modal structure. Loss of amplitude observed over 200 cm along isobaths (Figs. 4, 5) is not more than 5–10%, indicating an along-isobath e-folding decay scale L_d in the direction of propagation corresponding to about three wave-lengths, or 1950 cm, at a minimum. (In the next section it will be seen that wave amplitude loss between fields of view separated by 460 cm before and after a canyon also lies in a range centered on 10%, which, if there is minimal scattering by the canyon as is concluded below, suggests an even larger decay scale.) An estimate of L_d as $c_g T_d$, where c_g is the group velocity set by the slope of the dispersion curve (Fig. 7) and T_d the decay timescale, can also be made using the wave solution (Fig. 8) and the perturbation

method of Brink (1990) for determining T_d. The method parameterizes bottom stresses τ to be linear in bottom velocities $\mathbf{u}_B$ as $\tau = \rho_o r \mathbf{u}_B$, where r is the friction velocity constant, also called the bottom resistance parameter. Based on steady Ekman theory, in which the proportionality between τ and $\mathbf{u}_B$ magnitudes is $\rho_o(\sqrt{fKv/2})$, we use $r = \sqrt{fKv/2}$, = 0.025 cm/s, where K_V is molecular viscosity 0.01 cm^2/s as appropriate for the experiment. This use of steady Ekman layer behavior is not completely justified for the oscillatory perturbation analysis; it has been applied mainly for its convenience, and might be expected to result in an overestimate of the frictional influence. The result of the perturbation calculation, which uses the numerically determined modal structure (Fig. 8), is T_d = 404 s, which with c_g = 4.8 cm/s (Fig. 7) implies along-isobath e-folding scale 1930 cm. This is consistent at least with a lower bound for the experimentally observed decay length. The decay length L_d of the 180-cm wavelength mode at the forced frequency but on the second-gravest dispersion curve, as estimated similarly using the numerical solution and the bottom-stress parameterization, is substantially shorter at 113 cm. This is as expected by physical intuition, and in accord with the finding of little measured energy at wavenumbers other than the gravest mode (Section 3) because other modes dissipate significantly more quickly. In summary, while there is evidence of frictional signatures in the measured current ellipses, study of the gravest mode under weak dissipation is permitted since its damping occurs on a scale of at least a few wavelengths.

In addition to the dominant along-isobath propagation, experimental phase variations perpendicular to isobaths show a tendency for phase near the shelf break, where velocities are strongest, to lead that farther inshore and offshore (Fig. 9). Phases of both u and v reveal a systematic decrease along isobaths with distance from the wavemaker, as is consistent with wave propagation in this direction, and the phase difference between u and v at a given location is near the value of 90° expected for an inviscid wave. However, phase surfaces of the measured flow deviate significantly from lines perpendicular to isobaths, which would be the case in a purely inviscid wave, and reveal phase values near the shelf break that are high compared to farther onshore or offshore. This causes an apparent across-isobath horizontal phase propagation in the sense outward from the shelf break toward the shore and toward deeper water. This signature may be understood as a frictionally induced deviation from the inviscid free wave structure. The interpretation in terms of stratified trapped waves (Codiga, 1997) is that wave energy is moving toward the shelf break from both shallower and deeper water; this results from dissipation being strongest over the shelf break, which follows from the underlying wave mode having its maximum amplitudes there (Fig. 8) together with friction being proportional to flow strength. Qualitatively similar phase signatures, in which propagation is offshore away from stronger velocities in shallower water, have been seen in modeling of barotropic shelf waves with bottom friction (e.g. Power *et al.,* 1989). Evidence for such across-isobath phase propagation in field observations of subinertial topographic waves has been seen at Cobb Seamount (Codiga and Eriksen, 1997) and in coastal-trapped wave measurements along both east and west coasts of North America (Daifuku and Beardsley, 1983; Crawford and Thomson, 1984).

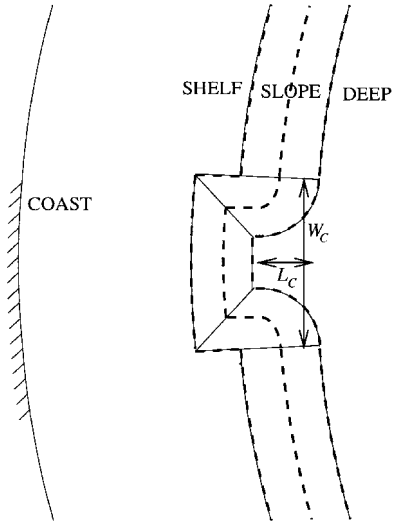

Figure 10. Canyon geometry, isobaths marked as heavy dashed lines.

Both the systematic current ellipse orientation at an angle to isobaths, and phase propagation across isobaths, are seen in the experiment to have the same senses as appear in ocean observations. In the laboratory the curvature along isobaths due to the cylindrical shape of the tank (isobaths are at constant radius from the axis of rotation, Fig. 3) might be expected to introduce asymmetries, though it is not clear what sense or strength this effect should have. Based on the fact that for both diagnostics discussed the asymmetries deviate from inviscid free wave behavior in the same sense as in numerically determined wave solutions under frictional influences (Codiga, 1997), we consider dissipation to be responsible.

5. Results: Wave incidence on canyon

In nature the continental slope and shelf are irregular on many scales, and submarine canyons commonly cause isobaths to be significantly distorted. In a step toward understanding the effect of bathymetry that is not uniform in the direction of wave propagation, this section describes results of an experiment where a trapped wave is incident on an idealized canyon.

As is appropriate to model a submarine canyon such as the Monterey Canyon or Hudson Canyon, in the experiment the canyon geometry (Fig. 10) is such that its width W_C along the continental slope is a small fraction of the along-isobath wavelength and its length L_C is of the same order as the width of the continental slope (Table 3). Within the experimental canyon, the continental slope is an inclined plane joining flat shallow water to flat deep water, in contrast to the cosine-squared profile present outside the canyon. Of course, a wide range of canyon shapes occur on the continental margins of the world and their effects

Table 3. Representative lengthscales of submarine canyon, and corresponding dimensionless numbers, in nature and experiment.

	Coastal Ocean	Experiment
Canyon width along coast, W_C	≈20 km	115 cm
Canyon length, L_C	≈30 km	40 cm
Canyon width/wavelength, W_C/λ	0.025	0.18
Canyon length/cont. slope width, L_C/L	1	0.8

on trapped waves may vary as a function of geometry; only a single canyon is studied here and sensitivity of the results to the specific canyon structure is not addressed. In this context, and given this limitation, we consider our results of interest despite the experimental exaggeration of W_C/λ relative to the representative scales chosen for Table 3. The canyon is positioned at a distance 850 cm from the wavemaker along isobaths (see Fig. 3). Results in this section are for wavemaker frequency $0.75f$ and amplitude $u_F = 1.9$ cm/s; the central experiment had frequency $0.8f$ and $u_F = 1.5$ cm/s (Table 1). The wave response prior to reaching the canyon (not shown), in a field of view centered at 605 cm from the wavemaker, has structure similar to that in Figure 6 and its amplitude is the same as in the central experiment when normalized relative to the forcing.

The incident wave field enters and leaves the canyon with its energy remaining concentrated over the sloping topography and its smooth phase progression continuing along isobaths (Figs. 11, 12). In the central frames of Figures 11 and 12 are current ellipses from time series at each individual location, calculated and shown as in Figure 5; the row of ellipses above (below) each central frame represents fits to along-isobath harmonics such as in Figure 6 but using data in a field of view centered over undistorted isobaths 245 cm before (215 cm after) wave incidence on the canyon, and with instantaneous velocities corresponding to the edge of this field of view that is nearest to the central frame. The similarities between current ellipses above and below the central frames in Figures 11 and 12 suggest that the wave structure after crossing the canyon has not been strongly changed from that before crossing it. Within the central frames of these figures, current ellipses along the axis of the canyon decrease in size, with distance toward deeper water from the head of the canyon, on a scale of about 40 cm as characterizes the decay across isobaths from the shelf break in waves away from the canyon (previous section). Contrasting the case without a canyon, in which uniform amplitudes of current ellipses are seen in Figure 5 along a column of the grid, along the corresponding grid columns in Figures 11 and 12 the ellipses within the canyon are relatively smaller. This may be understood in terms of the wave structure remaining concentrated over the sloping topography, entering and leaving the canyon with current amplitudes being preserved along isobaths. Continuous counterclockwise turning of the instantaneous velocity occurs along isobaths as well, indicating smooth phase propagation also follows the contours of the canyon.

The lack of significant energy at wavenumbers other than that of the primary along-isobath mode has been demonstrated based on the fact that the percent misfit variance in harmonic fits to the along-isobath propagating mode is not substantially higher than the

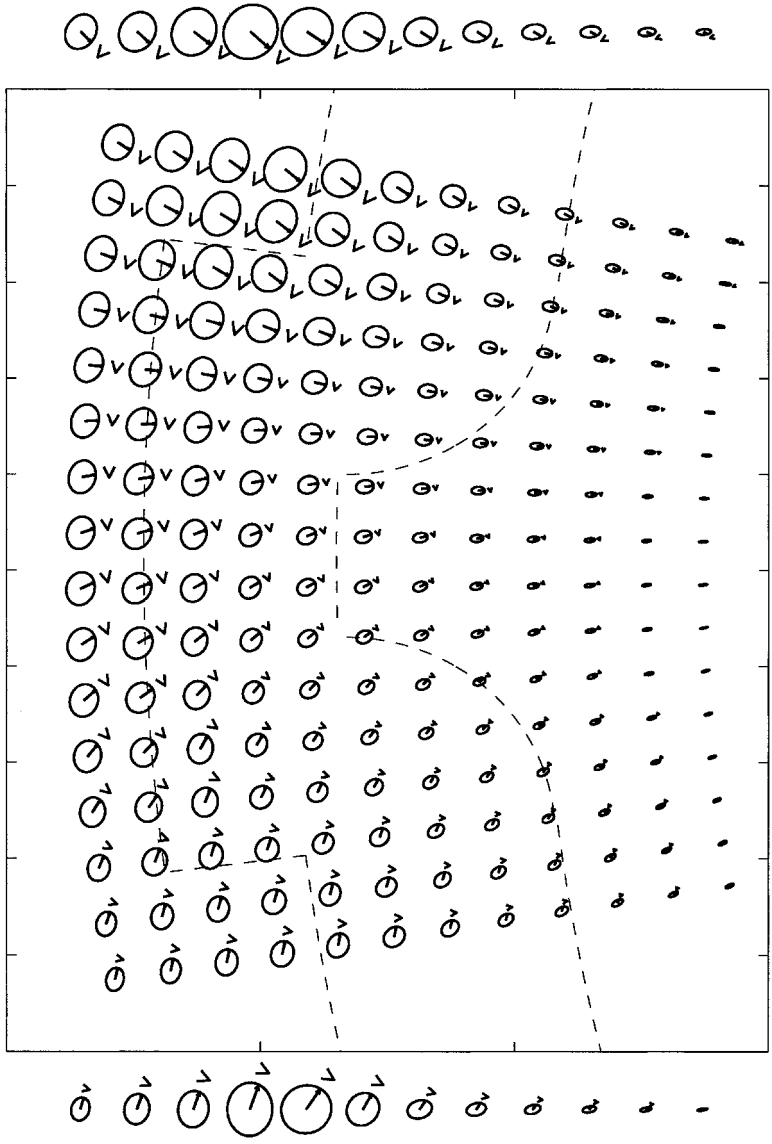

Figure 11. Current ellipses over the canyon at depth 1 cm shallower than the shelf, calculated as for Figure 5 with the same size field of view, with isobaths at the shallowest and deepest edges of the slope marked. Row of ellipses at top (bottom) results from along-isobath harmonic fits as in Figure 6 to flow over undistorted isobaths before reaching (after passing through) the canyon, in a field of view offset from that shown here by −245 cm (215 cm) along isobaths. Maximum velocity $0.31u_F = 0.59$ cm/s. Wave energy remains concentrated over the sloping topography, entering and leaving the canyon with weakly distorted phase progression, and transmits energy efficiently across the canyon.

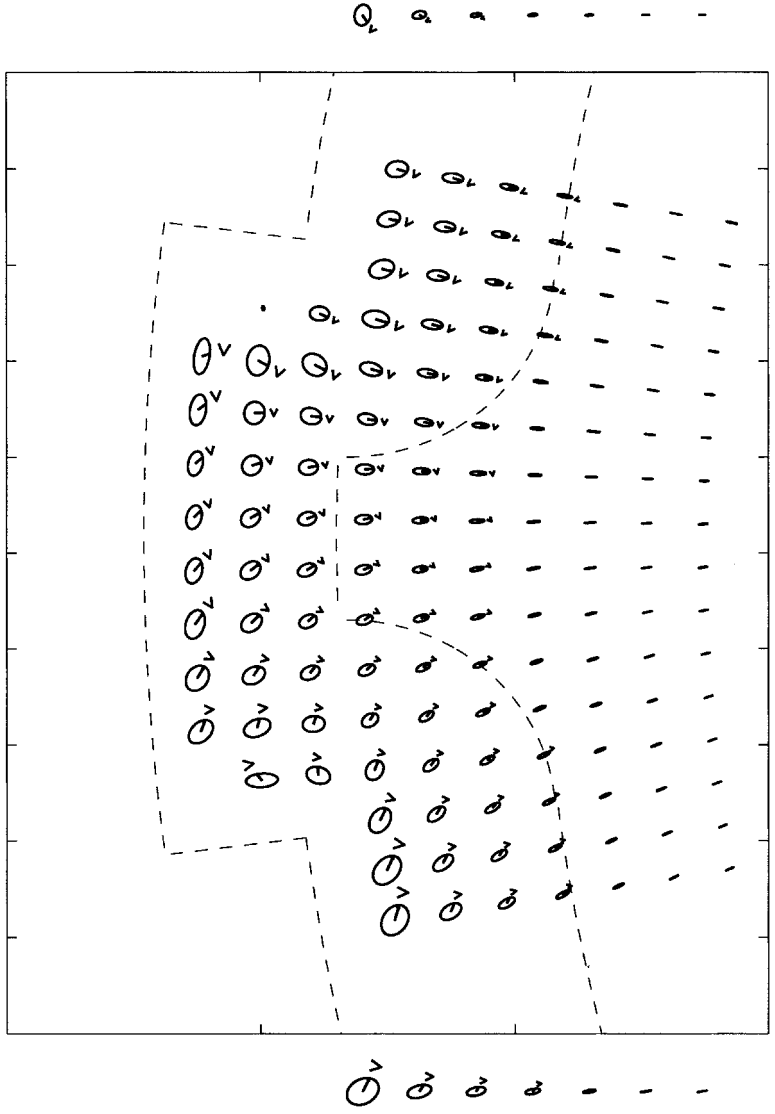

Figure 12. Identical to Figure 11 but at depth 1 cm deeper than the shelf.

percent misfit variance in time-dependent harmonic fits at individual locations (Section 3). This is true over the slope-shelf profile that does not change along isobaths, both prior to inclusion of the canyon and before and after incidence on it when it is present. If energy in scattered or evanescent waves was significant it would appear as a significantly increased misfit variance in the fit to the along-isobath harmonic, but this is not the case. In addition, the percent misfit variances in along-isobath fits lie in ranges that do not differ before and

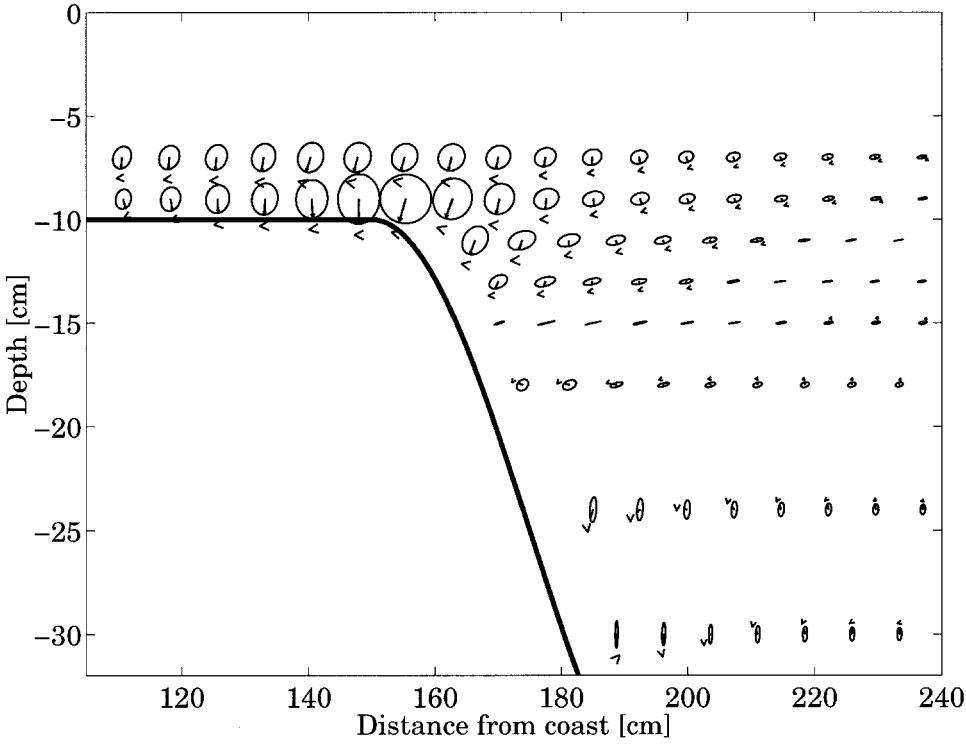

Figure 13. Current ellipse structure in the across-isobath/vertical plane calculated using data in a field of view centered at a distance 215 cm to the far side of the canyon from the wavemaker, plotted for direct comparison to Figure 6. Maximum velocity $0.31u_F = 0.59$ cm/s. Changes to the flow structure after transmission through the canyon are minor.

after canyon incidence. In the context of so little energy at other wavenumbers it is consistent to interpret the weak modification of the amplitude of the primary wavenumber on passing through the canyon, based on comparison of along-isobath fits over unchanging slope-shelf profile before and after canyon incidence, as a lack of scattering caused by interaction with the canyon. Weak scattering also accords with the significant wavenumber and frequency separation (Section 4) between the mode attributed to the measured signal and the nearest other modes on the dispersion curves (Fig. 7).

The three-dimensional structure of the wave after its transmission through the canyon (Fig. 13) is very similar to that prior to incidence (Fig. 6) and is further evidence that the canyon modifies waves only weakly. The wavenumbers determined by along-isobath harmonic fits along undistorted isobaths before and after canyon incidence are not substantially different, given the variation in values in the across-isobath/vertical plane (Section 4), showing increases of at most 15% on the downstream side. In addition, each of the current ellipse signatures described in Section 4 with no canyon present (Fig. 6) is

apparent downstream from the canyon (Fig. 13). The most strongly changed characteristic appears to be the vertical phase structure, as evidenced by instantaneous velocity orientation angles in the larger ellipses closest to the topography which are not as near to the 180° opposition between shallower and deeper depths of the free wave (Fig. 8) as they are prior to canyon incidence (Fig. 6). It is possible this is the signature of an additional wave that has resulted from the canyon interaction, which has a different wavenumber and/or is evanescent in the direction along isobaths, and is superposed on the primary wave; however, because such an additional wave does not significantly increase the misfit in the along-isobath harmonic fits, its amplitude must not exceed the basic level of measurement precision described in Section 3. We speculate that the changed features of the after-canyon wave structure, on further propagation away from the canyon, will be reduced as the flow returns to a structure more like that seen prior to canyon incidence.

Using the along-isobath harmonic fits centered over undistorted isobaths 245 cm before and 215 cm after incidence on the canyon (rows above and below the central frames in Figs. 11, 12), estimates of the transmission coefficient based on amplitude at a given position in the cross-isobath/vertical plane are in the range 0.9 ± 0.15. In addition to measurement limitations, the precision of these values is limited because the flow has strongest amplitudes occurring at different depths upstream and downstream. This explains the higher amplitudes downstream of the canyon at the deeper depth (Fig. 12), and accounts for transmission coefficients that exceed unity at certain locations in the across-isobath/vertical plane. An average transmission coefficient representative of the entire across-isobath/vertical plane has not be estimated owing to a lack of full sampling in the vertical both before and after the canyon. Some amplitude loss must be due to friction alone; the reasoning in the previous section, based on data from one 200-cm measurement field of view with no canyon present, suggests that between the measurements in before- and after-canyon fields of view separated by 460 cm the frictional loss would be 15%–20% at most. Thus the loss due to friction lies within the range of variation in the transmission coefficient estimates.

The transmission efficiency should be considered in light of the other potential outcomes that might reasonably have been expected of interaction with the canyon: significant reflection of energy, or amplification of waves to breaking, or scattering of energy to shallower and deeper water away from the slope, or forward-scattering of energy into higher along- or across-slope modes. There is no clear evidence for such behavior, and we find conversely that waves follow isobaths into and out of the canyon with coherent along-isobath structure that is much the same as seen along isobaths undistorted by the canyon.

6. Conclusions and discussion

As motivated by observations of coastal-trapped waves, we have performed rotating table experiments to simulate subinertial trapped waves over the continental slope and

shelf in a continuously stratified ocean. With regard to nearly all current ellipse diagnostics, the measured flow (Fig. 6) over uniform slope-shelf profile gives a very good qualitative match to the linear wave solution found numerically using laboratory parameters (Fig. 8). These diagnostics include maximum amplitudes that are concentrated near the bottom by the stratification, and also concentrated over the topographic slope that provides the boundary condition giving rise to the restoring force for the waves. The baroclinic vertical structure, rotation direction in time, and shapes of the current ellipses measured, in addition to the speed of phase propagation along isobaths, all agree with the linear solution.

The results prior to inclusion of the canyon represent a solid experimental confirmation of the already well-established coastal-trapped wave theory, and lend further credence to its continued application toward interpretation of low-frequency current observations in stratified coastal waters. There is good agreement of the combined forcing frequency and measured response wavelength with the corresponding values on the gravest dispersion curve (Fig. 7) determined by numerical solution of the linear wave equations for an along-isobath harmonic using laboratory parameters. Furthermore, the wave solution at this point on the dispersion curve shares many detailed characteristics of current ellipse patterns in the lab flow. Because current ellipse attributes are a wave diagnostic commonly collected in sea-going work, the success of this comparison suggests the possibility for further laboratory experiments to provide insights for the interpretation of field observations.

For example, the main difference between the experimental flow and the inviscid wave is an asymmetry in which horizontal current ellipse axes "tilt" ($\overline{uv} > 0$) as opposed to being locked parallel or perpendicular to isobaths; in addition, along a transect perpendicular to isobaths where phase would be constant in an inviscid wave, phase near the shelf break is found to lead phases closer to and farther from the coast (Fig. 9). These deviations from the free wave solution have been observed to have similar senses in ocean observations of coastal-trapped waves (Daifuku and Beardsley, 1983; Crawford and Thomson, 1984) and trapped topographic waves in stratification at a seamount (Codiga and Eriksen, 1997). An examination of diagnostic characteristics of wave solutions that include frictional damping (Codiga, 1997) has demonstrated that these differences from inviscid solutions result from dissipation acting on the waves.

We have found that waves incident on a canyon enter and leave it such that in the direction along isobaths current amplitudes are preserved and phase propagates smoothly, and transmit their energy across it efficiently. Motions at wavenumbers other than the primary along-isobath propagating mode have weak amplitudes that are not substantially different before or after canyon incidence, nor in the absence of the canyon; this indicates that transfers to scattered or evanescent waves as a result of interaction with the canyon are weak. Although a limited range of parameter space has been explored with respect to the canyon geometry, the implication of the efficient experimental transmission across the canyon is that in nature irregularities in the slope-shelf geometry will cause only weak

disruption of alongshore propagation and minimal scattering of energy out of a trapped wave mode.

An attempt can be made to place our experimental evidence for weak scattering by the canyon, and a velocity field that varies smoothly across it, in the context of previous theoretical (Johnson, 1991) and numerical modeling work (Wilkin and Chapman, 1990). Although the parameters in the experiment do not fall squarely within the ranges of any limiting case considered by Johnson (1991), they lie nearest to his strongly stratified case. For this limit the dynamics effectively reduce to internal Kelvin wave behavior and the theory indicates that scattering will be suppressed by the strong stratification. In this general sense, our results might be viewed as evidence in qualitative support of the theory. However, a puzzle arises on comparison of the experimental results with the numerical modeling of Wilkin and Chapman (1990), in which the scattering effect of isolated monotonic alongshore changes in shelf-slope structure is considered. There is little scattering in the laboratory experiment despite the fact that it incorporates strong bathymetric disruptions and stronger stratification than in the numerical work, where it was shown that both act to increase scattering. As regards the "shelf-similarity" (Hseuh, 1980) of the topography used here, given the concentration of wave energy over the shelf break and lack of importance of the coast, it does not seem appropriate to use the distance of isobaths to the coast in the definition of shelf-similarity. Use of distance of isobaths from the shelf break seems more appropriate, which together with the planar shape of the slope within the canyon (Section 5) leads to the conclusion that the canyon deviates quite strongly from shelf-similarity and, therefore, that strong scattering might be expected. In the strongly scattering cases of Wilkin and Chapman (1990) the amplitude lost by the incident mode reached about 15%, so it might have been expected that at least this much scattering would occur in the experiment. The experimental transmission coefficient is known marginally well enough to conclude that scattering more strongly than this did not occur. Furthermore, the rapid amplitude and phase variations which Wilkin and Chapman (1990) saw over the region of changing slope-shelf geometry are not seen in the experiment. There are many differences between their configuration and the experiment here, above and beyond the different numerical and laboratory methods, which might resolve the apparent discrepancy. For example, in the laboratory, the coastal wall is far removed from the slope, and there is a full canyon not simply a monotonic narrowing of the shelf. Nonetheless, it seems that the question of how irregularities in topography modify trapped waves in the presence of stratification, which is fundamental to extend the otherwise successful wave theory beyond one of its most restrictive assumptions, deserves more attention.

Acknowledgments. This project was made possible by the Chateaubriand Postdoctoral Fellowship Program through the Mission Scientifique et Technologique of the French Embassy. To have the continental slope and shelf, along with a broad range of other existing equipment, available in Grenoble was essential. We thank Henri Didelle and Rene Carcel for friendly and able engineering efforts, Geoff Spedding for programming assistance, Tetsu Hara for making software available, and

Ken Brink for comments on an earlier draft. The experiments could not have succeeded without the careful preparation of particles by Katie Faulkner at a critical time.

REFERENCES

Brink, K. H. 1990. On the damping of free coastal-trapped waves. J. Phys. Oceanogr., *20,* 1219–1225.

—— 1991. Coastal-trapped waves and wind-driven currents over the continental shelf. Ann. Rev. Fluid Mech., *23,* 389–412.

Brink, K. H. and D. C. Chapman. 1987. Programs for computing properties of coastal-trapped waves and wind-driven motions over the contintental shelf and slope, Technical Report 87-24, Woods Hole Oceanographic Institution, Woods Hole, MA.

Chapman, D. C. 1982. On the failure of Laplace's tidal equations to model subinertial motions at a discontinuity in depth. Dyn. Atmos. Oceans, *7,* 1–16.

Codiga, D. L. 1997. Physics and observational signatures of free, forced, and frictional stratified seamount-trapped waves. J. Geophys. Res., *102,* 23,009–23,024.

Codiga, D. L. and C. C. Eriksen. 1997. Observations of low-frequency circulation and amplified subinertial tidal currents at Cobb Seamount. J. Geophys. Res., *102,* 23,009–23,024.

Crawford, W. R. and R. E. Thomson. 1984. Diurnal-period continental shelf waves along Vancouver Island: a comparison of observations with theoretical models. J. Phys. Oceanogr., *14,* 1629–1646.

Daifuku, P. R. and R. C. Beardsley. 1983. The K1 tide on the continental shelf from Nova Scotia to Cape Hatteras. J. Phys. Oceanogr., *13,* 3–17.

Fincham, A. M. and G. R. Spedding. 1997. Low cost, high resolution DPIV for measurement of turbulent fluid flow. Exp. Fluids, *23,* 449–462.

Hseuh, Y. 1980. Scattering of continental shelf waves by variations in longshore bottom topography. J. Geophys. Res., *85,* 1,145–1,150.

Huthnance, J. M. 1978. On coastal-trapped waves: Analysis and numerical calculation by inverse iteration. J. Phys. Oceanogr., *8,* 74–92.

Johnson, E. R. 1991. The scattering at low frequencies of coastally-trapped waves. J. Phys. Oceanogr., *21,* 913–932.

Longuet-Higgins, M. S. 1968. On the trapping of waves along a discontinuity of depth in a rotating ocean. J. Fluid Mech., *31,* 417–434.

Power, S. B., J. H. Middleton and R. H. J. Grimshaw. 1989. Frictionally modified continental shelf waves and the subinertial response to wind and deep-ocean forcing. J. Phys. Oceanogr., *19,* 1486–1506.

Rhines, P. B. 1970. Edge-, bottom-, and Rossby waves in a rotating stratified fluid. Geophys. Fluid Dyn., *1,* 273–302.

Wilkin, J. L. and D. C. Chapman. 1990. Scattering of coastal-trapped waves by irregularities in coastline and topography. J. Phys. Oceanogr., *20,* 396–421.

Received: *6 October, 1998;* revised: *16 March, 1999*